Scanning Lidar Based Atmospheric Monitoring for Fluorescent Detectors of Cosmic Showers

D. Veberič [a,c,*], A. Filipčič [a,b], M. Horvat [a], D. Zavrtanik [a,b], M. Zavrtanik [a,b]

[a]*Nova Gorica Polytechnic, Laboratory for Astroparticle Physics, Vipavska 13, POB 301, SI-5001 Nova Gorica, Slovenia*

[b]*J. Stefan Institute, Department of Experimental Particle Physics, Jamova 39, POB 3000, SI-1001 Ljubljana, Slovenia*

[c]*J. Stefan Institute, Department of Theoretical Physics*

Abstract

Measurements of the cosmic-ray air-shower fluorescence at extreme energies require precise knowledge of atmospheric conditions. The absolute calibration of the cosmic-ray energy depends on the absorption of fluorescence light between its origin and point of its detection. We review a novel analysis method to reconstruct basic atmospheric parameters from measurements performed by the scanning backscatter lidar system. Applied inversion methods, optical depth, absorption and backscatter coefficient, as well as other parameters that enter the lidar equation are discussed in connection to the attenuation of the light traveling from the shower to fluorescence detector.

Key words: backscatter lidar, inversion methods, two- and multi-angle reconstruction, atmospheric optical depth, cosmic showers, fluorescent detectors
PACS: 42.68.Ay, 42.68.Jg, 42.68.Wt, 98.70.Sa

1 Introduction

Modern fluorescence experiments (Fly's Eye [1], HiRes [2], P. Auger [3]) studying cosmic rays with energies near $10^{20}\,e$V are/will detect fluorescence light produced along the air-shower volume through the atmosphere. Because fluorescence detection is essentially a calorimetric technique it is primarily sensitive to the electromagnetic (EM) component of the shower. EM component and hence the total

---

* Corresponding author.
  Email address: darko.veberic@ijs.si (D. Veberič).

number of low energy EM particles is in turn fairly accurately proportional to the energy of the primary cosmic ray. Thus, the calorimetric measure of the total EM shower energy [4] is proportional to the integral of EM particle density N_e along the shower direction x,

$$E_{\text{em}} = K \int N_e(x) \; \mathrm{d}x \qquad (1)$$

with $K \approx 2.2 \, \mathrm{MeV/g\,cm^2}$. E_{em} is a lower bound for the energy of the primary cosmic ray. Lower portion of shower development is usually obscured by the ground so that EM cascade reaching below ground is included by fitting a functional form to the observed longitudinal profile and integrating the function past surface depth. EM particle density $N_e(x)$ at the point x of their production is proportional to the number of photons N_{ph} reaching the fluorescence detector (FD),

$$N_e(x) \propto \frac{N_{\text{ph}} R^2(x)}{T(x)}, \qquad (2)$$

with $R(x)$ being line-of-sight shower–FD distance. Inclusively, number of detected photons is also corrected for the atmospheric transmission $T(x) < 1$,

$$T(x) = \exp\left[-\int_0^x \alpha(r) \; \mathrm{d}r\right] = \mathrm{e}^{-\tau(x)}, \qquad (3)$$

where $\alpha(r)$ is denoting volume extinction coefficient along the line-of-sight, while $\tau(x)$ stands for the resulting atmospheric optical depth (OD) to shower point x. Detected amount of light is thus reduced due to the absorption on molecules and aerosols in the atmosphere.

In the above sense, the atmosphere can be treated as an elementary-particle detector. However, weather conditions change the atmospheric transmission properties dramatically. Therefore, an absolute calibration system for fluorescence light absorption is the essential part of FD [5,6]. In order to lower primary cosmic ray energy uncertainties the volume extinction coefficient $\alpha(r)$ has to be well estimated over almost whole detection volume of FD, e.g., in the case of the Pierre Auger Observatory, the detection volume corresponds to the ground area of $3000 \, \mathrm{km^2}$ and the height of $\sim 15 \, \mathrm{km}$.

In this work we propose improved method for FD calibration based on scanning lidar system. In the next sections descriptions of lidar systems in general, specific experimental setup, lidar return simulation, test of established numerical methods for lidar problem inversion (only on simulated lidar returns), and novel two- and multi-angle methods will be given.

2 Lidar system

One of the most suitable calibration setups for FD is the backscattering lidar system, where a short laser light pulse is transmitted from FD position in the direction of interest. With help of a mirror and a photomultiplier tube a certain amount of backscattered light is collected and recorded as a function of time, i.e. function of distance. Note that light from lidar source traverses both directions, so that in case of matching laser and fluorescence light wavelength, OD for lidar light sums to twice the OD for fluorescence. Lidar equation [11] describes the received laser power $P(r)$ from distance r as a function of volume extinction coefficient $\alpha(r)$ and backscattering coefficient $\beta(r)$,

$$P(r) = P_0 \frac{ct_0}{2} \beta(r) \frac{A}{r^2} \, \mathrm{e}^{-2\tau(r)} \,. \tag{4}$$

P_0 is the transmitted laser power and A is the effective receiving area of the detector, proportional to the area of the mirror and the overlap between its field of view with the laser beam. t_0 is laser pulse duration. As seen from Eq. (2), measurement precision of α and corresponding OD τ directly influences the precision of primary cosmic ray energy estimation.

Simple as it may look, the lidar equation (4) is nevertheless tough on solving for two unknown variables, $\alpha(r)$ and $\beta(r)$. All existing analysis algorithms (Klett [7], Fernald [8], ...) reviewed in one of the following sections are based on experimental setup with static beam direction. This leads to ambiguity in determination of $\alpha(r)$ and $\beta(r)$ which can not be resolved without additional assumptions in atmospheric properties. For sites with FD experiments, the atmosphere can be safely assumed to be horizontally invariant. In this case, there is additional constraint when comparing signals coming from different directions, which solves the lidar equation for $\alpha(r)$ and $\beta(r)$ unambiguously. The need for steerable (scanning) lidar setup is therefore unavoidable for the proposed solution of lidar equation.

3 Experimental setup

The lidar system used for the analysis method verification is based on the Continuum MiniLite-1 frequency tripled Nd:YaG laser, which is able to transmit up to 15 shots per second, each with energy of 6 mJ and 4 ns duration (1.2 m). The emitted wavelength of 355 nm is in the $300 - 400$ nm range of fluorescence spectrum. The receiver was constructed using 80 cm diameter parabolic mirror with focal length of 41 cm. The mirror is made of aluminum coated pyrex and protected with SiO_2.

The backscattered light is detected by a Hammamatsu R7400 photomultiplier with operating voltage up to 1000 V and gain of $\sim 10^6$. To suppress background, a
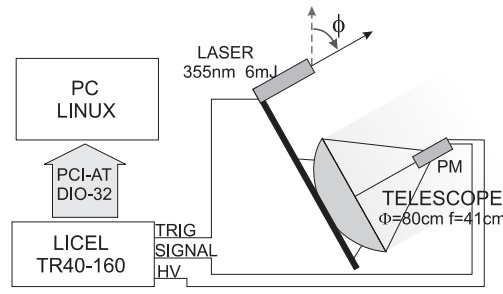
Figure 1. Schematic view of the lidar system. A mirror of 80 cm diameter and UV-laser head are mounted on the steerable mechanism. The LICEL TR40-160 receives the trigger from the laser and the signal from Hammamatsu R7400 phototube. The Linux-PC controls the LICEL digitizer through PCI-DIO-32HS Digital Input/Output card. The steering motors are controlled through RS-232 port. Zenith angle is denoted by ϕ.

broadband UG-1 filter with 60% trasmitance at 353 nm and FWHM of 50 nm is used.

The distance between laser beam and the mirror center is fixed to 1 m, allowing in this way the system to be fully steerable with $0.1°$ angular resolution.

The signal is digitized by three-channel LICEL transient recorder TR40-160 with 12 bit resolution at 40 MHz sampling rate with 16k trace length combined with 250 MHz fast photon counting system. The maximum detection distance of this hardware setup is around 60 km. LICEL is operated by PC-Linux system through National Instruments digital input-output card (PCI-DIO-32HS) with Comedi drivers [9] and ROOT DAQ interface [10].

4   Lidar simulation with specific atmospheric model

In low opacity atmosphere the attenuation and backscattering coefficient can be written as a sum of contributions from two independent components,

$$\alpha(h) = \alpha_{\mathrm{m}}(h) + \alpha_{\mathrm{a}}(h), \tag{5a}$$
$$\beta(h) = P_{\mathrm{m}}(180°)\alpha_{\mathrm{m}}(h) + P_{\mathrm{a}}(180°)\alpha_{\mathrm{a}}(h). \tag{5b}$$

where α_{m} and α_{a} correspond to the molecular and aerosol attenuation, respectively. The aerosol phase function $P_{\mathrm{a}}(180°)$ for backscattering has next to wavelength also a strong dependence on optical and geometrical properties of the aerosol particles. Nevertheless, at wavelength of 355 nm, values in the range 0.025 and up to $0.05\,\mathrm{sr}^{-1}$ can be assumed [11] for aerosol phase function $P_{\mathrm{a}}(180°)$. The angular dependence of molecular phase function is based on Rayleigh scattering, where $P_{\mathrm{m}}(180°) = 3/8\pi\,\mathrm{sr}^{-1}$.

For simulation purposes, the elevation dependence of the extinction coefficients is

4
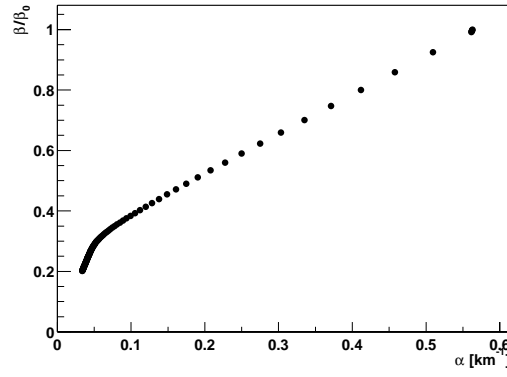
Figure 2. Extinction–backscatter plot ($\alpha\beta$ diagram) for the model atmosphere in Eq. (6).

modeled as following,

$$\alpha_{\mathrm{m}}(h) = \frac{1}{L_{\mathrm{m}}}\,\mathrm{e}^{-h/h_{\mathrm{m}}^{0}}, \tag{6a}$$

$$\alpha_{\mathrm{a}}(h) = \frac{1}{L_{\mathrm{a}}} \begin{cases} 1, & h < h_{\mathrm{x}} \\ \mathrm{e}^{-(h-h_{\mathrm{x}})/h_{\mathrm{a}}^{0}}, & h \geq h_{\mathrm{x}}. \end{cases} \tag{6b}$$

where L_{m} and L_{a} are the molecular and aerosol attenuation lengths at ground level, h_{m}^{0} and h_{a}^{0} are the molecular and aerosol scale height, respectively. Additional mixing height h_{x} is set up for aerosols, allowing their uniform concentration near the ground level.

This atmospheric model (6) serves as a testing ground for two widely used reconstruction methods presented in next section. Comparison with reconstructions of the real atmosphere yields insight into the common problems of the lidar field. Correct Poissonian statistics of photon counting and multiplying, background noise, and effects of digitalization have been taken into account in the generation of the simulated lidar signals and match those observed in the real lidar power returns.

Model (6) is a valid approximation to the atmospheric conditions found in real experiments. Although vertical variation of aerosol and molecular densities is quite simple the model still produces nontrivial relation between total attenuation α and total backscattering coefficient β. Therefore, the relation $\beta(\alpha)$, shown in Fig. 2, can not be well approximated by some fundamental functional form.

5   Reconstructions of 1D atmosphere

Concentrating on a single shot lidar measurement, the optical properties have to be reconstructed in a 1D subspace of the atmosphere. Rewriting the lidar equation (4),

$$P(r) = B\frac{\beta(r)}{r^2}\,\mathrm{e}^{-2\tau(r)} \tag{7}$$

and collecting system's effective aperture in constant B, an auxillary S-function can be introduced,

$$S(r) = \ln \frac{P(r)r^2}{P(r_0)r_0^2} = \ln\left[\beta(r)/\beta_0\right] - 2\tau(r; r_0). \tag{8}$$

Note that $\tau(r; r_0) = \int_{r_0}^{r} \alpha(r') \, dr'$ corresponds to atmospheric OD between ranges r_0 and r.

5.1 Klett inversion

Apart from the experimentally measured lidar power return $P(r)$, in Eq. (7) there are two unknown quantities, β and α (or equivalently τ), preventing the unique solution of the lidar equation. Nevertheless, a simple and sometimes physically meaningful assumption of proportionality between backscattering and extinction,

$$\beta(r) \propto \alpha^k(r), \tag{9}$$

allows for the transformation of the integral Eq. (8) to the corresponding Bernoulli's differential equation with existing analytical solution. Direct application of the solution (forward inversion) is numerically unstable, in some cases singular, and highly sensitive to the signal noise [7,12]. Klett's reformulation [7] of the solution (backward inversion) solves these problems. Lidar backward inversion algorithm proceeds from the far point of the measured signal r_f to the bottom,

$$\alpha(r; \alpha_f) = \frac{e^{S(r)/k}}{e^{S_f/k}/\alpha_f + \frac{2}{k}\int_r^{r_f} e^{S(r')/k} \, dr'}, \tag{10}$$

where $S_f = S(r_f)$, and $\alpha_f = \alpha(r_f)$ is an estimate for the attenuation at the far end of the data set. Reconstructed attenuation $\alpha(r; \alpha_f)$ is still an one-parameter function of the unknown boundary attenuation value α_f, so that independent measurement or suitable approximation is needed at the reference distance r_f. OD can be expressed directly from Eq. (10),

$$\tau(r; r_0, \alpha_f) = \frac{k}{2} \ln\left[\frac{k\, e^{S_f/k} + 2\alpha_f \int_{r_0}^{r_f} e^{S(r')/k} \, dr'}{k\, e^{S_f/k} + 2\alpha_f \int_r^{r_f} e^{S(r')/k} \, dr'}\right]. \tag{11}$$

Whole inversion method rather strongly depends on assumed power law proportionality in Eq. (9). In Fig. 4, a failure of this approximation is demonstrated for the specific atmospheric model used for our simulations. Local value of the exponent,

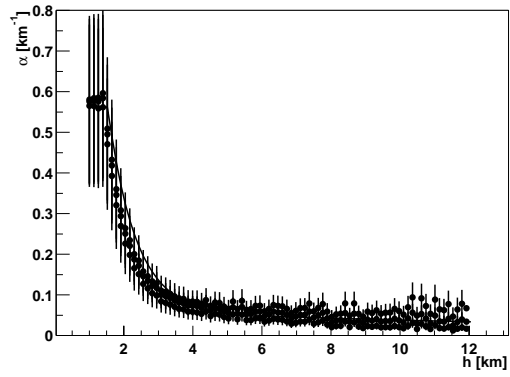$$k = \frac{\alpha}{\beta}\frac{d\beta}{dr}\left[\frac{d\alpha}{dr}\right]^{-1}, \tag{12}$$

6

Figure 3. Reconstructed attenuation $\alpha(h)$ from Klett's inversion of the simulated vertical shot data as obtained by different boundary values α_f. Solutions with 0.5, 1, and 2 times the correct α_f are plotted with dots. The actual model α profile is drawn with solid line. Assuming range-independent (constant) Klett's k, the best agreement between the reconstructed and actual profile is achieved for $k \approx 0.5$, so that this value is used for all tree plots.
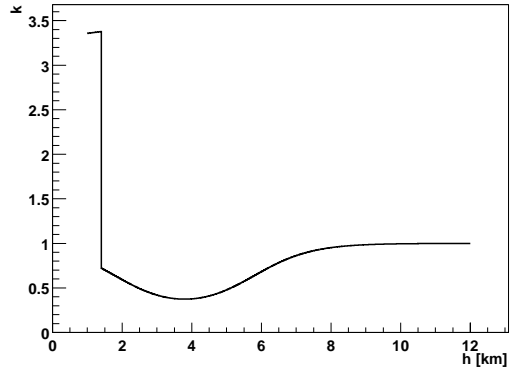

Figure 4. Effective power k in Eq. (9) as obtained from the model atmosphere in Eqs. (5) and (6).

is shown to posses substantial range dependence. The main reason for failure of the power law proportionality stems from the inequality of the molecular and aerosol phase functions, $P_m(180°)$ and $P_a(180°)$, rendering α and β relationship dependent on the particular magnitude of both quantities and thus range dependent (see Fig. 2). Therefore, the best value of k must be chosen by some *ad hoc* method.

From the results in Fig. 3 presenting Klett inversion of simulated lidar signals, it seems that the closest reconstruction of the model profile is achieved with $k \approx 0.5$. From Fig. 4 showing local exponent k obtained with use of Eq. (12), it can be seen that $k \approx 0.5$ is observed only in small interval around $4\,\mathrm{km}$ whereas at other places it is substantially larger. For $r > 8\,\mathrm{km}$ dominated by molecular scattering it slowly approaches in the literature most commonly used value of 1. Nevertheless, as can be seen in Fig. 5, reconstruction of OD with $k = 1$ totally fails to reproduce correct answer. Surprisingly, in case of this specific atmospheric model the most authentic result is obtained with $k \approx 0.5$.
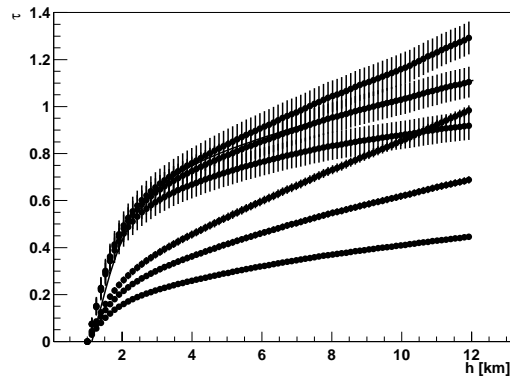
Figure 5. Reconstructed optical depth $\tau(h; h_0)$ from Klett inversion in Fig. 3 (with 0.5, 1, 2 times the correct boundary α_f). Upper three curves are obtained using $k = 0.5$ and lower three with most frequently used $k = 1$. The actual model τ profile is drawn with solid line (and is well covered by the middle curve with $k = 0.5$).

Another drawback of the Klett's method is estimation of the extinction α_f at the far end of the lidar return. In case that r_f corresponds to high elevation point, approximation $\alpha_f \equiv \alpha_m(r_f)$, i.e. the extinction at that point is dominated by the molecular scattering, yields quite reasonable results [13] with qualitative convergence to the correct α-profile. Generally, for optically dense atmosphere (presence of moderate haze) convergence of the Klett's method is far more rapid as in clear, optically thin case. Quite opposite, sites for FD are usually chosen at locations with clear and cloudless atmosphere. For horizontal lidar measurements (zenith angle $\phi = 90°$) in horizontally invariant atmosphere, α_f can be estimated as the one that minimizes extinction deviations from constant value [13,14], i.e. minimizes the functional $\int_{r_0}^{r_f}[\alpha(r') - \alpha_f]^2 \, dr'$.

5.2 Fernald inversion

Since concentration of the molecules depends solely on the thermodynamic parameters of the atmosphere, e.g. density, the Rayleigh scattering on molecules is modeled separately on a basis of the meteorological data. $\alpha_m(r)$ acquired in that way is inserted in Eq. (5). With an estimate for the molecular and aerosol backscattering phase fraction, $F = P_m(180°)/P_a(180°)$, and modified S-function

$$\tilde{S}(r) = S(r) + 2(F - 1) \int_r^{r_f} \alpha_m(r') \, dr', \tag{13}$$

the lidar equation can be solved for aerosol part $\alpha_a(r)$ following the same steps as Klett's version,

$$\alpha_a(r) = -F\alpha_m(r) + \frac{e^{\tilde{S}(r)}}{e^{\tilde{S}_f}/\tilde{\alpha}_f + 2\int_r^{r_f} e^{\tilde{S}(r')} \, dr'}, \tag{14}$$
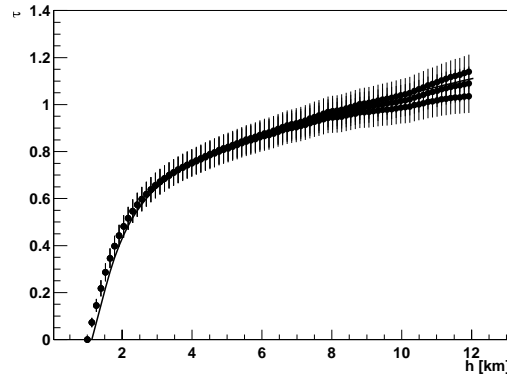
8

Figure 6. Fernald inversion of simulated lidar signal. Correct result is drawn in solid line. The three data sets are inversions with $\alpha_a(r_f) = 0$ and $\pm\alpha_m(r_f)/2$. F is kept equal to the value used for generation of simulated lidar returns.

with $\tilde{\alpha}_f = F\alpha_m(r_f) + \alpha_a(r_f)$ and $\tilde{S}_f = \tilde{S}(r_f) = S(r_f)$. In the same way OD is expressed as

$$\tau(r; r_0, \tilde{\alpha}_f) = \frac{1}{2}\ln\left[\frac{e^{\tilde{S}_f} + 2\tilde{\alpha}_f \int_{r_0}^{r_m} e^{\tilde{S}(r')} \, dr'}{e^{\tilde{S}_f} + 2\tilde{\alpha}_f \int_{r}^{r_m} e^{\tilde{S}(r')} \, dr'}\right] +$$
$$+ (1 - F)\int_{r_0}^{r} \alpha_m(r') \, dr'. \tag{15}$$

Note that the Fernald procedure relies on three independently supplied parameters: accurate guess of molecular part of the scattering $\alpha_m(r)$ along the whole range of interest, total extinction at the far end $\tilde{\alpha}_f$, and proper approximation for phase fraction F. As predicted by the Mie theory, it is quite difficult to obtain reasonable values for the latter. As of $\tilde{\alpha}_f$, conclusions are similar to those of Klett's α_f.

In Fig. 6 Fernald's inversion of simulated lidar return is shown for different input values of $\alpha_a(r_f)$ that enter total extinction $\tilde{\alpha}_f$. For upward pointing lidar measurements vanishing aerosol concentration can be assumed at the far end of atmosphere, i.e. $\alpha_a(r_f) = 0$. To test the sensitivity of the reconstructed OD on this assumption, data sets with $\alpha_a(r_f) = \pm\alpha_m(r_f)/2$ and therefore $\tilde{\alpha}_f = (F \pm 1/2)\alpha_m(r_f)$, are also plotted. $P_a(180°) = 0.025\,\text{sr}^{-1}$ is used for phase fraction F. Comparing to the Klett's method which does not separate aerosol and molecular scattering, it is not surprisingly that the variation of Fernald's results on boundary parameters is somewhat weaker. Pinning the molecular part of scattering undoubtedly stabilizes obtained OD profiles. Nevertheless, Fernald's inversion still relies heavily on additional external parameters that are usually difficult or almost impossible to measure.

9

6 Horizontally invariant atmosphere

Fluorescence detectors for cosmic showers are usually placed at locations with specific atmospheric conditions. In case of Pierre Auger Observatory, the FD cameras are covering lower part of the atmosphere over an almost perfect $3000\,\mathrm{km}^2$ plane $1500\,\mathrm{m}$ above the see level with remarkable year fraction of cloudless days. Due to the high elevation and dry inland climate optically thin atmosphere is expected. But as noted before, in that case convergence of Klett's method is slower and can lead to erroneous assessments of OD. Based on that and other peculiar problems of the well established lidar inversion methods new approach with less *ad hoc* or hard-to-estimate input parameters is needed. Since lidar equation is not uniquely solvable, a minimal set of assumptions needed for inversion has to be reconsidered. For a typical FD site it is quite reasonable to assume horizontal invariance of the atmospheric optical properties. That is even more true for a huge plane mentioned above, with hardly any variations in elevation and vegetation coverage. Furthermore, mean night wind speeds do not exceed $12\,\mathrm{km/h}$ [15], so that only a thin layer of aerosols close to the ground is expected. At night, it is also counted on low probability for formation of convective type of atmospheric instabilities.

6.1 *Two-angle reconstruction*

Under moderate assumptions presented above, optical parameters of atmosphere that enter the lidar equation (7) can be assumed to posses only vertical variation while being uniform and invariant in the horizontal plane.

Thus, it makes sense to rewrite the range dependent S-function in Eq. (8) in terms of height h and geometric factor $\xi = 1/\cos\phi = \sec\phi$, when lidar shots with zenith angle ϕ are considered. The S-function becomes

$$S(h, \xi) = \ln\left[\beta(h)/\beta_0\right] - 2\xi\,\tau(h; h_0) \qquad (16)$$

with "vertical" OD $\tau(h; h_0) = \int_{h_0}^{h} \alpha(h')\,\mathrm{d}h'$. After measuring two S-functions at different zenith angles $\xi_1 = 1/\cos\phi_1$ and $\xi_2 = 1/\cos\phi_2$ but fixed height h, Eq. (16) can be solved for vertical OD,

$$\tau(h) = -\frac{1}{2}\frac{S(h, \xi_1) - S(h, \xi_2)}{\xi_1 - \xi_2}, \qquad (17)$$

and backscatter coefficient ratio,

$$\frac{\beta(h)}{\beta_0} = \exp\left[-\frac{\xi_2 S(h, \xi_1) - \xi_1 S(h, \xi_2)}{\xi_1 - \xi_2}\right]. \qquad (18)$$
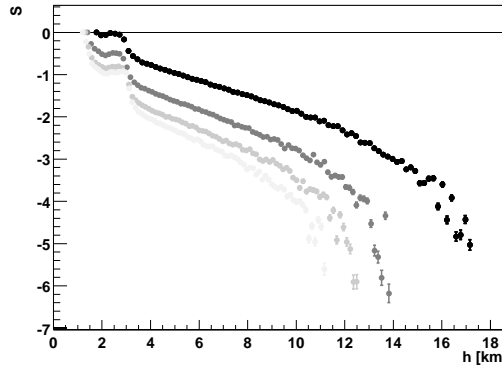
Figure 7. S-function at few angles, $\phi = 0°$ (black), $38°$, $42°$, and $47°$ ($\xi = 1, 1.27, 1.35,$ and 1.47), in shades of gray.

Both quantities are directly proportional to the difference of two S-functions at the same hight and different angles. Therefore, choosing a small separation between zenith angles, i.e. geometrical factors $\xi_1 = \xi$ and $\xi_2 = \xi + \mathrm{d}\xi$, a differential form of Eq. (17) can be written,

$$\tau(h) = -\frac{1}{2}\frac{\partial S}{\partial \xi}\bigg|_h.\tag{19}$$

Equivalently, differential form of Eq. (18) can be obtained easily,

$$\frac{\beta(h)}{\beta_0} = \exp\left[S(h,\phi) - \xi\frac{\partial S}{\partial \xi}\bigg|_h\right].\tag{20}$$

Note that OD is in that way determined up to the additive constant and backscatter coefficient up to the multiplicative factor. Nevertheless, both are linked to satisfy $S(h_0) = 0$ and $\tau(h_0) = 0$.

Taking into account the Poissonian statistics of collected photons and neglecting all other sources of measurement uncertainties, a relative error of the obtained OD at some height depends on the lidar system parameters,

$$\frac{\sigma_\tau}{\tau} = \frac{h/h_0}{2\tau\sqrt{N_0\tilde{\beta}}} \cdot \frac{1}{|\xi_1 - \xi_2|}\sqrt{e^{2\xi_1\tau} + e^{2\xi_2\tau}},\tag{21}$$

as well as relative error of backscatter coefficient

$$\frac{\sigma_\beta}{\beta} = \frac{h/h_0}{\sqrt{N_0\tilde{\beta}}} \cdot \frac{\sqrt{\xi_2^2\,e^{2\xi_1\tau} + \xi_1^2\,e^{2\xi_2\tau}}}{|\xi_1 - \xi_2|},\tag{22}$$

where N_0 is number of detected photons in time interval corresponding to the power return from height h_0, and $\tilde{\beta} = \beta/\beta_0$.

In Fig. 7 an example of S-functions and their zenith angle variation is presented. All results are obtained from real lidar measurements performed in few November
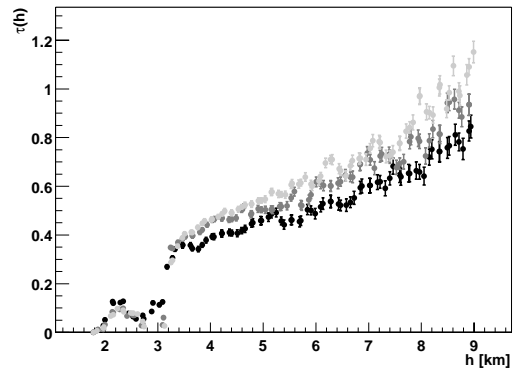
11

Figure 8. Reconstructed optical depth (OD) τ from pairs of S-functions in Fig. 7. In all pairs, S_1 corresponds to the S-function with $\phi = 0°$ ($\xi = 1$).
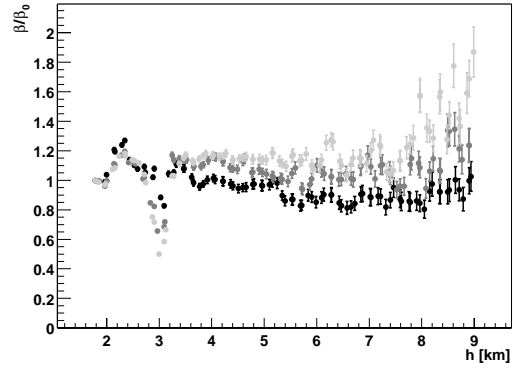

Figure 9. Reconstructed backscatter coefficient $\beta(h)/\beta(h_0)$ from pairs of S-functions in Fig. 7.
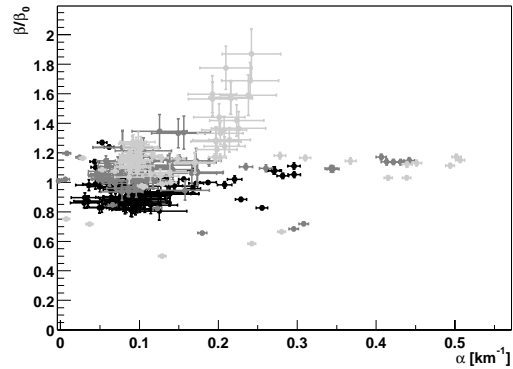

Figure 10. $\alpha\beta$ diagram (extinction-to-backscatter plot). Compare with model $\alpha\beta$ diagram in Fig. 2.

nights in a typical urban atmosphere (GPS location:). For fixed $\phi_1 = 0°$ and three selected azimuth angles $\phi_2 = 38°$, $42°$, and $47°$ results for OD (Fig. 8), backscatter coefficient (Fig. 9), and $\alpha\beta$ diagram (Fig. 10) are obtained from corresponding S-functions in Fig. 7. Due to presence of a thin layer of optically thick haze at $h \approx 3$ km wild change in both OD and backscattering at that height is observed. Since OD is well determined only up to additive constant, note that the variation of results for different ϕ_2 is easily produced by inadequate determination of S_0, in
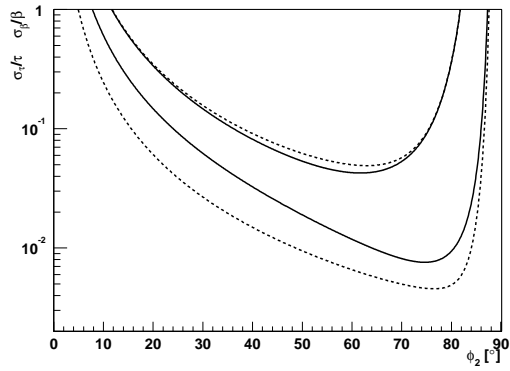
12

Figure 11. Logarithmic plot of the relative deviation in OD, σ_τ/τ (solid line), and backscattering coefficient, σ_β/β (dashed line), vs. the second shot angle ϕ_2, in case that the first shot zenith angle is set to $\phi_1 = 0°$. Values $h/h_0 = 8$, $N_0 = 4 \cdot 10^6$, $\tau = 1$, and $\beta/\beta_0 = 0.6$ corresponding to the far point ($h \approx 8$ km) in Fig. 8 have been assumed for parameters in Eqs. (21) and (22) (upper two curves). Values $h/h_0 = 3$, $N_0 = 4 \cdot 10^6$, $\tau = 0.4$, and $\beta/\beta_0 = 0.8$ corresponding to the near point ($h \approx 2$ km) are assumed for the lower two curves. Note that $\phi = 60°$ corresponds to $\xi = 2$.

other terms by variation of atmospheric optical properties at h_0. Compatible with scale height of ~ 18 km, the variation of backscattering in Fig. 9 is slower as found in our model, generating gradual but still comparable $\alpha\beta$ diagram in Fig. 10.

In Fig. 11 logarithmic plot of the relative error in OD is presented for typical lidar system parameters. First angle is fixed to $\phi_1 = 0°$ while the second one, ϕ_2, is varied from vertical to almost horizontal shot. It is hard to avoid the fact that minimum error is produced with evaluation of two quite considerably separated lidar shots, $\phi_2 \approx 70°$. Even at moderate elevations h this can amount to large spatial separations of the two points of lidar return, and thus the requirement of horizontal invariance easily broken. In case of horizontally slowly modulated atmosphere more "local" approach to the OD problem is needed.

6.2 Multi-angle reconstruction

For the ideal atmosphere with true horizontal invariance, the ξ dependence of S-function is particularly simple,

$$S(h, \xi) = \ln[\beta(h)/\beta_0] - 2\xi \, \tau(h; h_0), \tag{23}$$

with backscatter coefficient $\ln[\beta/\beta_0]$ as offset, and OD τ as slope of the resulting linear function in ξ. Therefore, optical properties of the atmosphere can be alternatively obtained from the analysis of the S-function behavior for scanning lidar measurements. Furthermore, disagreement of the measured $S(\xi)$ profiles from the linear form is a suitable criterion for detection of deviations from the assumed horizontal invariance of the atmosphere.
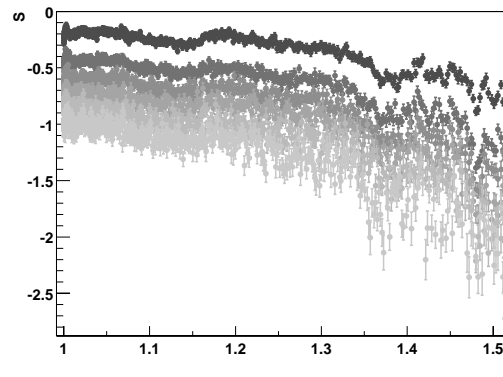
13

Figure 12. Dependence of S-function at various heights on azimuth angle. Starting with dark data points, $h = 3.2, \ldots 7\,\mathrm{km}$, while $h_0 = 3\,\mathrm{km}$. Note that $\xi = 1$ corresponds to $\phi = 0°$, and $\xi = 1.5$ to $\phi = 48°$.
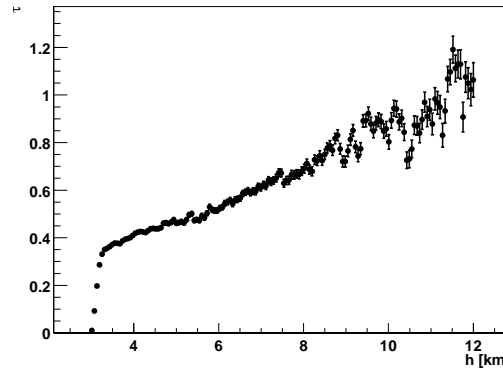

Figure 13. Optical depth τ obtained by linear fits of angle dependence of S-functions in Fig. 12.

Generalization of the two-angle equations (19) and (20) to their differential counterparts strongly hinted at this way of reconstruction of the optical properties, the two-angle method being a mere two-point approximation of the linear function in Eq. (23). Taking into account quite substantial uncertainties in $S(\xi)$ for single angle, the linear fit trough many data points seems to yield superior results and the reconstruction is no longer limited to taking two in angle well-separated lidar shots. Condition of horizontal invariance is not required to take place across huge atmospheric volumes (as in case of two $\phi = 0°$ and $60°$ shots), but has to be met only in relatively small arc of interest where continuous lidar scan is performed.

In opposite case of slow variation in horizontal plane, Eq. (19) is not quite, but similar enough to the renown 1D "slope method" used with assumption of small variation of $\beta(r)$, or equivalently $\mathrm{d}\beta/\mathrm{d}r \approx 0$. Bear in mind that in method presented here the variation of β with height can be of any magnitude, as long as there are only modest variations along the horizontal plane.

Opposite to Fig. 7, in Fig. 12 S-function profiles with respect to zenith ξ are drawn for fixed heights, starting with $h = 3.2\,\mathrm{km}$ and up to $7\,\mathrm{km}$ with $633\,\mathrm{m}$ step. Approximate linear behavior is observed in few arc intervals, with narrow bands of minute
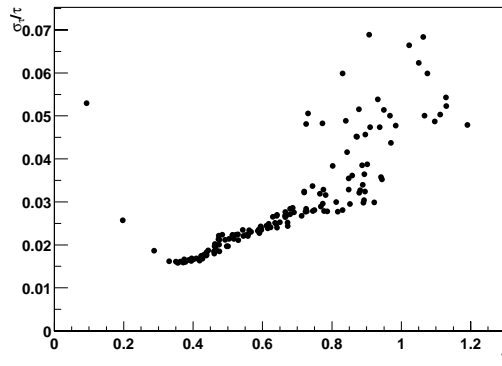
14

Figure 14. Dependence of relative error in optical depth on depth itself, σ_τ/τ. Data points and uncertainties are from Fig. 13.
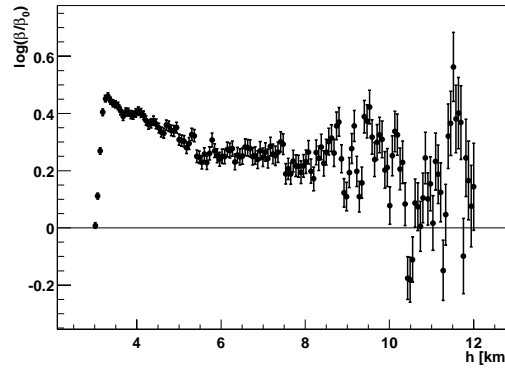

Figure 15. Relative backscattering coefficient $\beta(h)/\beta_0$ from S-functions in Fig. 12.

atmospheric shifts at $\xi = 1.15$ and 1.38. Since these shifts in profiles disappear when lifting h_0 from 3 km to 3.5 km, they are obviously due to the distortions of atmosphere in the latter interval, feature already observed in Fig. 8.

In Fig. 13 results of fitting and extraction of OD are similar to the ones in Fig. 8. Note that in both cases OD is obtained relative to the h_0 point, so that the results may differ up to some additive constant. Therefore, comparing both figures it is more accurate to concentrate on the same span of OD in the 3.5 km to 9 km interval. Nevertheless, the range of OD results with acceptable error bars is with multi-angle method increased up to 12 km.

Relative error of OD in Fig. 14 is needed for correct estimation of shower energy uncertainty. It is kept below 6% even for the OD from the far points of the range, and below 3% for modest values of OD. Fig. 15 with values for β/β_0 should be compared to Fig. 9.

15

7 Conclusions

Inversion attempts of simulated lidar returns for atmosphere, modeled by Eqs. (6), show numerous drawbacks of established numerical methods. For instance, Klett's and Fernald's method of section 5.1 and 5.2 do not satisfy the specific requirements of FD calibration. While they may be useful for qualitative reconstruction of atmospheric properties (spatial haze/cloud distribution, cloud base etc.), they are not applicable for absolute assessment of atmospheric transmission properties. There are many reasons for this failure. One of them is certainly strong dependence of obtained inversions on presumed extinction/backscatter functional relation, Eq. (9), in case of Klett's method, and assumed spatial dependence of Rayleigh scattering on molecules in Fernald's case. Another issue is the next-to-impossible measurement of far-side extinction rate α_f, needed in Eq. (10), and phase fraction F, Eq. (13). We are therefore forced to find better solutions, even for the expense of adding scanning capabilities to otherwise rigid lidar setup.

In contrast to that, based on sole assumption of horizontally invariant (or at least horizontally slowly varying) atmosphere the two- and especially the multi-angle method presented in section 6, while simple in structure, nevertheless produce strong quantitative answers with small uncertainties (e.g., see Figs. 8 and 13) to FD calibration questions. Furthermore, concerning the specific form of the atmospheric transmission entering Eq. (2), they offer suitable starting ground for development of methods that even further reduce systematic errors of shower energy estimation.

Acknowledgements

References

[1] R.M. Baltrusaitis et al., Nucl. Instrum. Methods A **240**, 410 (1985); Phys. Rev. Lett. **54**, 1875 (1985).

[2] T. Abu-Zayyad et al., Proc. 25th ICRC **5**, 321 (1997); ibid. **5**, 325 (1997); ibid. **5**, 329 (1997).

[3] D. Zavrtanik, J. Phys. G: Nucl. Phys. **27**, 1597 (2001).

[4] *Pierre Auger Observatory Design Report*, Second Edition, Auger Collaboration (1997).

[5] I. Arčon, A. Filipčič, and M. Zavrtanik, Pierre Auger Collaboration note GAP-1999-028, Fermilab (1999).

[6] D.J. Bird et al., *Atmospheric Monitoring for Fluorescence Detector Experiments* in Proc. 24th ICRC (1995).

[7] J.D. Klett, Appl. Optics **20**, 211 (1981); ibid. **24**, 1638 (1985).

[8] F.G. Fernald, Appl. Optics **23**, 652 (1984).

[9] Comedi, *Linux control and measurement device interface*, `http://stm.lbl.gov/comedi` (2001).

[10] ROOT, *An Object-Oriented Data Analysis Framework*, `http://root.cern.ch` (2001).

[11] R.T.H. Collis and P.B. Russell, *Lidar Measurement of Particles and Gases by Elastic Backscattering and Differential Absorption* in *Laser Monitoring of the Atmosphere*, edited by E.D. Hinkley, p. 88 (Springer, 1976).

[12] F. Rocadenbosch and A. Comerón, Appl. Optics **38**, 4461 (1999).

[13] M. Horvat, *Measurement of atmospheric optical properties with lidar system*, graduate thesis (Ljubljana, 2001).

[14] T. Yamamoto et al., *Telescope Array atmospheric monitoring system at Akeno Observatory* in Proc. 27th ICRC (2001).

[15] P. Bauleo et al., Pierre Auger Collaboration note GAP-1998-041, Fermilab (1998).

[16] J.A.J. Matthews, Pierre Auger Collaboration note GAP-2001-046, Fermilab (2001); ibid. GAP-2001-051.

[17] J.A.J. Matthews and R. Clay, *Atmospheric Monitoring for the Auger Fluorescence Detector* in Proc. 27th ICRC (2001).

[18] B. Dawson, Pierre Auger Collaboration note GAP-2001-016, Fermilab (2001).

[19] R. Cester, M. Mostafá, and R. Mussa, Pierre Auger Collaboration note GAP-2001-099, Fermilab (2001).